

Field and experimental constraints on the rheology of arc basaltic lavas: the January 2014 Eruption of Pacaya (Guatemala)

A. Soldati¹ · A. Sehlke^{1,2} · G. Chigna³ · A. Whittington¹

Received: 6 October 2015 / Accepted: 18 April 2016 / Published online: 20 May 2016
© Springer-Verlag Berlin Heidelberg 2016

Abstract We estimated the rheology of an active basaltic lava flow in the field, and compared it with experimental measurements carried out in the laboratory. In the field we mapped, sampled, and recorded videos of the 2014 flow on the southern flank of Pacaya, Guatemala. Velocimetry data extracted from videos allowed us to determine that lava traveled at ~ 2.8 m/s on the steep $\sim 45^\circ$ slope 50 m from the vent, while 550 m further downflow it was moving at only ~ 0.3 m/s on a $\sim 4^\circ$ slope. Estimates of effective viscosity based on Jeffreys' equation increased from ~ 7600 Pa s near the vent to $\sim 28,000$ Pa s downflow. In the laboratory, we measured the viscosity of a representative lava composition using a concentric cylinder viscometer, at five different temperatures between 1234 and 1199 °C, with crystallinity increasing from 0.1 to 40 vol%. The rheological data were best fit by power law equations, with the flow index decreasing as crystal fraction increased, and no detectable yield strength. Although field-based estimates are based on lava characterized by a lower temperature, higher crystal and bubble fraction, and with a more complex petrographic texture, field estimates and laboratory measurements are mutually consistent and both indicate shear-thinning behavior. The complementary field and laboratory data sets allowed us to

isolate the effects of different factors in determining the rheological evolution of the 2014 Pacaya flows. We assess the contributions of cooling, crystallization, and changing ground slope to the 3.7-fold increase in effective viscosity observed in the field over 550 m, and conclude that decreasing slope is the single most important factor over that distance. It follows that the complex relations between slope, flow velocity, and non-Newtonian lava rheology need to be incorporated into models of lava flow emplacement.

Keywords Viscosity · Rheology · Morphology · Lava flow · Pacaya

Introduction

Lava rheology and morphology

The interpretation of lava morphology requires a detailed understanding of how its physical properties vary as it flows away from the source vent, cooling and crystallizing along the way. Important physical properties of lavas include viscosity (η) and yield strength (σ_y), both of which depend on temperature (T) and crystal fraction (Φ_c) (e.g. Spera 2000). The crystal fraction itself varies with T , along with the residual liquid composition (X), and all three factors (T , X , Φ_c) are important in controlling lava viscosity. Thermodynamic models such as MELTS (Ghiorso and Sack 1995) allow the prediction of crystal fraction and residual liquid composition of a lava if thermodynamic equilibrium were maintained during flow emplacement. However, experimental work is necessary to overcome the discrepancy between model output and natural occurrences, as lava flow cooling often entails disequilibrium crystallization.

Editorial responsibility: M.R. Patrick

✉ A. Soldati
arianna.soldati@mizzou.edu

¹ Department of Geological Sciences, University of Missouri, Columbia, MO, USA

² NASA Ames Research Center, Moffett Field, CA, USA

³ Instituto Nacional de Sismología, Vulcanología, Meteorología e Hidrología, Guatemala City, Guatemala

Viscosity data for silicate liquids as a function of temperature are usually fit with a non-Arrhenian Vogel-Tamman-Fulcher (VTF) equation (Vogel 1921) of the form

$$\log_{10}\eta = A + B/(T-C) \quad (1)$$

where A represents theoretical viscosity at infinite temperature, B is an activation energy, and C is a temperature term. Empirical viscosity models are now available to predict liquid viscosities as a function of temperature and composition (Hui and Zhang 2007; Giordano et al. 2008), although they are not necessarily able to predict the viscosity evolution of the melt during crystallization with the accuracy required for lava flow modeling (e.g. Sehlke et al. 2014). As magma crystallizes, certain elements are preferentially removed from the melt phase, which is therefore typically driven to a more silica-rich composition, more viscous than the original melt.

A variety of rheological behaviors, described by constitutive relations linking the applied force (shear stress, σ) and resulting deformation rate (strain rate, $\dot{\gamma}$), can be observed in magma under different conditions. The simplest relation is Newtonian behavior, in which a straight line whose slope is the material viscosity (η) goes through the origin

$$\sigma = \eta\dot{\gamma} \quad (2)$$

Silicate melts are Newtonian, except at very high strain rates (Webb and Dingwell 1990). However, several experimental studies (e.g. Shaw et al. 1968; Ryerson et al. 1988) demonstrated that lavas are shear-thinning, as the presence of crystals and bubbles alters their rheological behavior, which is then best described by the Herschel-Bulkley constitutive relation

$$\sigma = K\dot{\gamma}^n + \sigma_y \quad (3)$$

where K [Pa s] is the consistency, i.e. the effective viscosity at a strain rate of 1 s^{-1} and σ_y [Pa] is the yield strength, i.e. the strength which needs to be overcome before flow is initiated. If no yield strength is present, the constitutive relation is referred to as power law.

We use the term *effective viscosity* to refer to the ratio of stress to strain rate observed either in the field or in the laboratory, while acknowledging that the behavior of lava and other suspensions is rarely Newtonian. The rheology of two-phase (melt + crystals and melt + bubbles) lavas was recently reviewed by Mader et al. (2013). Many issues are still debated in the field of lava rheology, including the existence of a yield strength (Ryerson et al. 1988; Ishibashi 2009), the rate of increase of effective viscosity with crystal fraction (Ishibashi and Sato 2010; Costa et al. 2009), and the influence of crystal size and shape distribution on effective viscosity and shear-

thinning behavior (Mueller et al. 2011; Cimarelli et al. 2011; Faroughi and Huber 2014). Furthermore, lavas are typically three-phase materials, containing both rigid crystals and deformable bubbles, leading to further complexity in rheological behavior depending on their relative sizes (e.g. Phan-Thien and Pham 1997; Truby et al. 2015).

The micro-scale physical properties of lava, such as crystal and bubble content, control its rheological properties (viscosity and yield strength), which in turn determine the macroscopic flow surface morphometry (Hulme 1974). These parameters vary along and across the lava flow through space and time (Griffiths 2000), with the final morphology of the flow recording the last stage of these variations. For example, Hawaiian basalts typically erupt as hot, crystal poor, fast-flowing pahoehoe lavas characterized by a smooth and ropey surface texture, which downstream cool and crystallize leading to the morphological transition to rough and blocky `a`a (e.g. Peterson and Tilling 1980; Hon et al. 2003; Robert et al. 2014). Similar transitions have been observed in basaltic lava flows at other volcanoes, including Pacaya (Guatemala), the focus of this study.

The viscosity of an active lava flow can be inferred from Jeffreys' equation (Jeffreys 1925)

$$\eta = (g\rho(\sin\alpha)d^2)/(3v) \quad (4)$$

where η [Pa s] is the viscosity, g [m/s^2] the gravitational constant, ρ [kg/m^3] the bulk density, α [$^\circ$] the flow slope, d [m] the flow depth, and v [m/s] the surface flow velocity. Jeffreys' equation is designed to calculate the viscosity of a Newtonian fluid, as that is effectively the ratio of stress to strain rate. In the case of non-isothermal lava flows containing crystals and/or bubbles, this is a simplifying yet useful assumption. Furthermore, Jeffreys' equation is based on a sheet of fluid flowing down a uniform slope, not on a channelized flow. As shown by Lev and James (2014), Jeffreys' equation may overestimate the viscosity of a flow occurring in a channel of unknown geometry. However, when estimating the viscosity of active flows, the uncertainty arising from estimation of flow depth is typically larger than that associated with channel geometry. Therefore, Jeffreys' equation provides a useful first-order viscosity estimate.

A synergy of optical flow analyses of the flow velocity field and numerical models is capable of generating more accurate rheological results, but its application to natural lava flows may be challenging (Lev et al. 2012).

Although in the field of rheology the existence of yield strength is not universally accepted (e.g. Barnes 1999), large-scale lava flow morphology has traditionally been interpreted through yield strength (Hulme 1974). When a flow is no longer active, yield strength can be estimated from lava

flow thickness, because the critical thickness h_c required for flows to advance depends on σ_y (Hulme 1974)

$$h_c = \sigma_y / \rho g \tan \alpha \quad (5)$$

Levéé width w depends on the same parameters (Hulme 1974)

$$w = \sigma_y / 2 \rho g \alpha^2 \quad (6)$$

Sparks et al. (1976) noted that yield strength estimates may depend on the equation chosen to obtain them: flow thickness-based estimates are consistently slightly higher than levée width-based estimates for narrow channels.

Integration of field- and laboratory-based constraints on lava rheology

Few studies previously compared field- and laboratory-based rheological measurements of lava flows. Gauthier (1973) conducted field measurements of Etna lavas viscosity using observed flow velocity and steel spear insertion ($\eta=260$ Pa s at 1130 °C) and laboratory measurements with rotating cylinder viscometry ($60 < \eta < 400$ Pa s). A yield strength of 4.5–30 Pa was detected at the liquidus (1200 °C). Pinkerton and Norton (1995) measured the viscosity of Etna lavas using a rotating vane viscometer ($1385 < \eta < 1630$ Pa s at 1095 °C) and laboratory measurements using concentric cylinder viscometry in a reducing atmosphere at unit strain rate ($\eta=150$ Pa s at 1125 °C to $\eta=3000$ Pa s at 1084 °C). The detected maximum yield strength was 78 Pa at 1087 °C. Fink and Zimbelman (1986) calculated viscosity and yield strength values for tholeiitic basalts from Kilauea, using levée height and width and ground slope by applying the methods developed by Hulme (1974) and Moore et al. (1978), which assume a Bingham rheology ($\eta=2 \cdot 10^5$ Pa s at 1127 °C to $\eta=8.2 \cdot 10^6$ Pa s at 1094 °C). Their yield strength estimates were 1500–50,000 Pa, in agreement with laboratory values measured in the 1150–1100 °C temperature range. We infer that field- and laboratory-based viscosity estimates are consistent and can therefore be valuably combined. Here, we investigate the rheology of basaltic lavas from Pacaya, Guatemala, which threaten human settlements and coffee plantations on the volcano slopes.

Tectonic setting and recent activity

Pacaya belongs to the Central American Volcanic Arc, generated by the subduction of the Cocos Plate underneath the Caribbean plate. Pacaya is currently in the third phase of its eruptive history (Eggers 1971), which built the currently active MacKenney Cone through basaltic lava flows and tephra

emissions over the past 23 ky. An arcuate collapse scarp (2000–400 years ago; Vallance et al. 1995) forms a topographic barrier to most lava flows along its western side. The current cycle of activity began in 1961 after nearly a century of repose, and so far consists of eight distinct eruptions through 2013 (Rose et al. 2013), with the January 2014 eruption being the ninth. Further details on the eruptive history of Pacaya can be found in Eggers (1971), Bardintzeff and Deniel (1992), Matías Gomez (2009), and Rose et al. (2013).

On January 9th 2014, following a few hours of strombolian activity, Pacaya emitted two lava flows from different vents, one on the west side and one on the south side. The vents are aligned along a NNW-trending crack traversing the volcano's summit, which developed during the May 2010 eruption (Schaefer et al. 2013). The western flow was extremely short-lived, lasting only 3 days, while the southern flow remained active until April 15th 2014. The western flow came to a halt after 2.5 km, while the southern flow reached a total length of 4.2 km. Despite its constant unrest and its proximity to major cities, the only previous rheological investigation of Pacaya lavas was by Bollasina (2014), who measured the rheology of lavas emitted during the 2010 eruption. Our goal in this study was to accurately characterize the rheological behavior of the 2014 Pacaya lavas through laboratory experiments, to compare these results with field-based estimates, and to assess the roles of different factors such as cooling, crystallization, and ground slope in affecting the rheological behavior of the lava along the flow.

Methods

Field observations

We conducted fieldwork at Pacaya in January 2014, shortly after the beginning of the eruption. A total of 18 lava samples were collected (Table 1), 16 from along the middle of the channel and the levées of the western and southern 2014 flows, and 2 quenched directly at the active front of the southern flow, which did not advance further after our field campaign (Fig. 1). We recorded sample locations using a handheld Garmin eTrex GPS. In combination with the GPS, a TruPulse 360R laser rangefinder was used to make longitudinal and transverse topographic profiles of both flows.

Several videos of the active southern flow were acquired with a Canon EOS T1i DSLR camera, from a location near the vent looking down onto two different sections of the flow, from the ancient collapse scarp, and from a flow levée further downstream, for a total of three different flow sections. Videos were captured at 1020 × 780 pixel resolution at 20 fps. The flow velocity was then calculated with the free software Tracker[®] 4.87, using naturally occurring lava blocks transported on top of the flow as tracer particles. Tracker[®]

Table 1 Location (UTM coordinates, WGS84; UTM zone 15P) of collected samples

Flow	Sample	Easting m	Northing m	Elevation m	Vent distance m	Notes
Southern	14PA04	0758584	1589556	1601	550	Abandoned channel
	14PA05	0758260	1589555	1548	880	W levée
	14PA06	0758260	1589555	1548	880	W breakout lobe
	14PA01	0757880	1588730	1406	1650	W lobe front
	14PA03	0757876	1588730	1541	1655	W levée
	14PA17	0757229	1587292	1227	3420	Active lobe (quenched)
	14PA18	0756716	1587160	1157	4210	Active front (quenched)
	14PA19	0756716	1587160	1157	4210	Active front slab
Western	14PA07	0758382	1591861	2148	90	Spatter
	14PA08	0758335	1591845	2271	240	Lobe margin
	14PA09	9758135	1591876	2216	470	S levée
	14PA10	0758153	1591904	2220	470	Main channel
	14PA11	0757740	1592062	2131	910	S levée lobe
	14PA12	0757731	1591998	2120	910	Main channel
	14PA13	0757731	1591998	2120	910	Main channel
	14PA15	0756803	1591789	1716	1850	Main channel
	14PA16	0756801	1591774	1719	1850	S levée
	14PA14	0756214	1592001	1661	2490	Flow front

refers to a chosen model frame in order to identify the feature of interest (in our case the rafted block) in subsequent frames and provide its spatial coordinates. A sampling rate of 5 fps was chosen to eliminate the effects of video instability. Video frame scale was calibrated using distances between the recording location and reference points across and along the flow channel, which were measured using the laser rangefinder. Consequently, distance traveled has an uncertainty of ~25 %, while time is known very precisely.

Density measurements and porosity calculations

The density (ρ) of each sample was measured with each of the following three different techniques: (1) pycnometric (ρ_{DRE}), (2) geometric (ρ_g), and (3) Archimedean (ρ_A). The 2σ precision given below is based on five repeat measurements of one powder batch or one rock core per sample. Pycnometry allows accurate measurement of the volume of a known mass of powder by displacing a known pressure of gas (helium) and then applying the Boyle-Mariotte law. The obtained density measurement is a dense rock equivalent (DRE) density, because it expresses the density of the solid part of the sample only. The technique has a 2σ precision better than 50 kg/m^3 , or better than 2 % of the average pycnometric density value. Geometric density is obtained by measuring the height and diameter of a cylindrical sample with a micrometer, and then dividing the calculated volume by its mass. Geometric density is therefore a bulk density, including both the solid part of the sample and the bubbles trapped inside it. The technique has a 2σ precision better than 20 kg/m^3 , or better than 1 % of the

average geometric density value. The Archimedean density is obtained by measuring the mass of a sample in air, and subsequently while immersed in anhydrous ethanol. This includes the solid part of the sample and only the isolated bubbles, since porosity is efficiently penetrated by ethanol during the pre-measurement 12 h immersion period. The technique has a 2σ precision better than 200 kg/m^3 , or better than 8 % of the average Archimedean density value. The lower precision of this technique probably reflects variably effective penetration of sample porosity by ethanol. The combination of these three density measurements allowed us to calculate the total (Φ_{tot}), interconnected (Φ_{int}), and isolated porosity (Φ_{is}) with the following relationships (Avard and Whittington 2012):

$$\Phi_{tot} = 1 - \left(\rho_g / \rho_{DRE} \right) \quad (7a)$$

$$\Phi_{int} = 1 - \left(\rho_g / \rho_A \right) \quad (7b)$$

$$\Phi_{is} = \left(\rho_g / \rho_A \right) - \left(\rho_g / \rho_{DRE} \right) \quad (7c)$$

Rheology experiments: sample preparation

Sample 14PA04 was chosen as the experimental starting material. It is the sample collected closest to the SE vent and its bulk chemistry typifies that of all the collected samples.

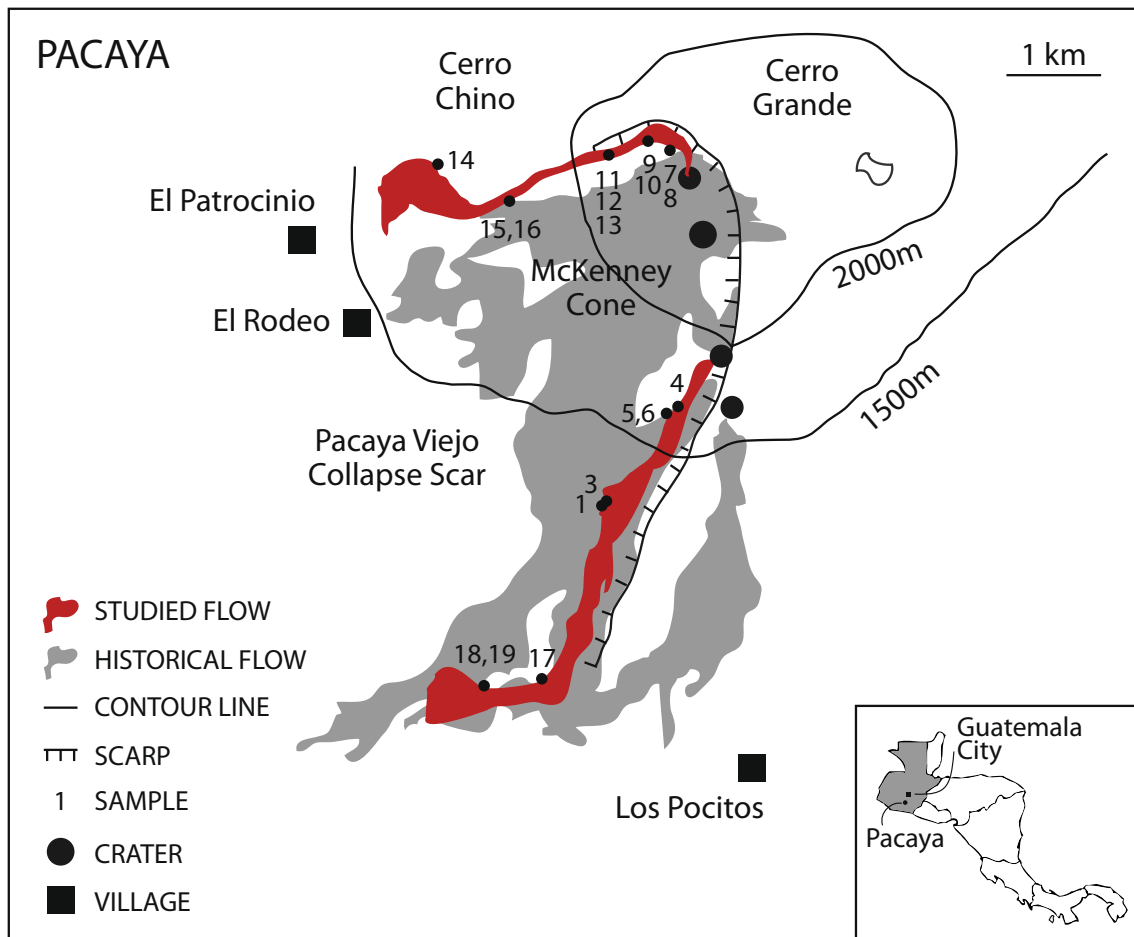


Fig. 1 Aerial map of Pacaya based on CONRED (COordinadora Nacional para la REDucción de Desastres; www.conred.gob.gt) maps and laser rangefinder measurements. 2014 lava flows are highlighted in

red, and their source vents are shown. Older flows outline based on Rose et al. 2013. Location of collected samples is also indicated

14PA04 was crushed and melted in an iron-saturated Pt₉₀-Rh₁₀ crucible inserted in an MHI Z-series box furnace. The sample was melted in air for 1 h at 1600 °C and splat-quenched on a copper plate. The resulting glass was again crushed, melted, and quenched with the same procedure in order to ensure homogenization of the sample. The resulting glass was used to perform all viscosity tests.

Additionally, we synthesized a glass (14PA04evo) corresponding to the composition of the interstitial, evolved melt of the lowest temperature (1199 °C) subliquidus experiment. The synthesis was done from oxide and carbonate powders in the MHI box furnace, following the same homogenization procedure as for the natural (remelted) sample.

Parallel plate viscometry

Viscosity of cylindrical cores (diameter Ø=6.6 mm, height 5 mm < h < 10 mm) of glass was measured by uniaxial compression in a Theta Industries Rheotronic III parallel plate viscometer, over the ~10⁸ Pa s to ~10¹² Pa s range. The load

used was 1500 g, and the applied stresses ranged from 3.79 · 10⁵ Pa to 4.12 · 10⁵ Pa. The temperature was measured with a K-type thermocouple positioned next to the sample core. The viscometer was checked against NIST standard glasses, indicating an accuracy of better than 0.06 log units (Whittington et al. 2009). Sample longitudinal deformation over time data were collected at alternating higher and lower temperatures, in order to detect possible sample crystallization, which would have resulted in a deviation from the trend of previous measurements during the same experiment in a log viscosity vs. inverse temperature plot. The maximum shortening of the glass cores was 6.8 %.

Assuming perfect slip, the stress (σ) is calculated as:

$$\sigma = \frac{Mg}{V/h} \tag{8}$$

where M [kg] is the load, g [m/s²] the gravitational constant, V [m³] the volume of the sample, and h [m] the sample height (Dingwell 1995).

The volumetric strain rate ($\dot{\gamma}$) is calculated from the relation:

$$\dot{\gamma} = 3 \frac{\Delta h/h}{\Delta t} \quad (9)$$

Resulting strain rates ranged between $1.33 \cdot 10^{-7} \text{ s}^{-1}$ and $1.26 \cdot 10^{-4} \text{ s}^{-1}$.

The effective viscosity is then obtained as the ratio of stress to volumetric strain rate.

Concentric cylinder viscometry

A Theta Industries Rheotronic II Rotating viscometer was used to perform both superliquidus and subliquidus experiments. We used a Brookfield DV3TRV Rheometer measuring head for liquid experiments and a Brookfield HBDV-III Ultra measuring head for subliquidus measurements. Both are able to measure in the 10^{-1} – 10^5 Pa s viscosity range, depending on spindle geometry and immersion depth; however, the HBDV-III Ultra has a stronger full range spring torque ($57,496 \cdot 10^{-4}$ Nm) compared to the Brookfield DV3TRV ($7187 \cdot 10^{-4}$ Nm), which enables a wider range of viscosity values to be obtained at the greater strain rates (and therefore greater torques) characteristic of subliquidus experiments. The sample was placed in an iron-saturated Pt₉₀-Rh₁₀ cylindrical crucible ($h=65$ mm; ID=30.125 mm) held stationary in the furnace by three alumina rods. Temperature was measured with an Al₂O₃-sheathed S-type thermocouple positioned outside the bottom of the crucible. An alumina spindle covered by an iron-saturated Pt₉₀-Rh₁₀ sleeve with a flat tip ($h=65$ mm; OD=3.75 mm) was immersed in the melt to a depth of about 20 mm via an attached micrometer, and made to rotate at selected speeds by the measuring head. After the experiment, the spindle was raised out of the melt, and the actual immersion depth was verified by measuring the residual melt covering the Pt₉₀-Rh₁₀ sleeve.

The computer records torque values as percentages of the maximum spring torque of the used measuring head.

The stress (σ) is then calculated as

$$\sigma = \frac{M}{2\pi(r_s^2 l)} \quad (10)$$

where M [N m] is the measured torque, r_s [m] the spindle radius, and l [m] the measured spindle immersion depth.

The strain rate ($\dot{\gamma}$) is calculated from the relation

$$\dot{\gamma} = \frac{2\omega}{n \left(1 - (r_s/r_c)^{2/n}\right)} \quad (11)$$

where ω [rad/s] is the angular velocity of the spindle, r_c [m] the crucible inner radius, and n the flow index. The flow index is

the slope of the measured τ against ω on a double natural logarithmic plot. A flow index value of 1 indicates Newtonian behavior, whereas a value of less than 1 indicates shear-thinning behavior.

The effective viscosity is then obtained as the ratio of stress to strain rate.

Liquid experiments started by reaching a temperature of 1550 °C, which was then decreased stepwise by 25 °C at a time (~1 h per step) until crystallization was detected at 1150 °C, both as a deviation from the viscosity predicted from earlier measurements and as a non-Newtonian rheological response of the material. The temperature was increased again to 1550 °C as the last experimental step, so as to certify that no instrumental drift took place. At each temperature, measurements were made at three different angular velocities in order to verify the Newtonian behavior of the melt. No significant (>2 °C) temperature gradient was detected when moving the thermocouple up and down along the crucible height, indicating that the measured temperature is representative of the entire sample.

Subliquidus experiments started by equilibrating the melt at 1500 °C for 30 min, in order to ensure the absence of crystals, which was also verified by checking the liquid viscosity against the viscosity measurements previously obtained at the same temperature. Afterwards, the melt was cooled at a rate of 10 °C/min until the target temperature was reached. The melt was then left to equilibrate at that temperature for at least 12 h. About 10 viscosity measurements were subsequently performed at constant temperature but different angular velocities (0.4–20 rpm), each one lasting 30 min. No slip between the spindle and lava was detected during any of the experiments. At the end of the experiment the spindle was raised out of the melt, and the crucible was rapidly removed from the assembly and quenched in a water bath. We expect that the crystallinity observed in quenched products reflects that at experimental conditions.

Samples were extracted from the crucible by drilling cores with a 25 mm diameter drill bit, and polished sections were prepared from the recovered material. The same crucible was then used for the next subliquidus experiment. A few grams of the originally homogenized glass were added to replace the material drilled out after each experiment.

Chemical analysis

Bulk rock chemical analyses were performed by Inductively Coupled Plasma Optical Emission Spectroscopy (ICP-OES) at Actlabs Inc. (Ontario, Canada). Calibration was performed using one of 7 USGS and CANMET certified reference materials during the analysis for every group of ten samples.

The microscopic composition of post-experiment samples was analyzed at Washington University in St. Louis on a JEOL JXA-8200 electron microprobe equipped with five

wavelength-dispersive spectrometers (WDS) and a JEOL (e2v/Gresham) silicon-drift energy-dispersive spectrometer (EDS). Operating conditions were 15 kV accelerating potential and 25 nA probe current for a 5 μm beam diameter. Silicate and oxide standards were used for calibration, and data were corrected with CITZAF (Armstrong 1995). A minimum of five individual analyses were performed on each glass, and at least three individual analyses were obtained for each crystal phase (plagioclase, oxides) in every sample.

Evaluation of phase volume fractions

In order to quantify the crystal fraction at each subliquidus experiment, both radial and longitudinal sections of the crucible contents were analyzed. Several backscattered electron images (BSE) were acquired at 50x magnification. Crystallinity estimates of subliquidus experimental runs were obtained by processing a minimum of 3 BSE images of radial and longitudinal sections of each experiment with the free software JMicroVision[®] in order to quantify the crystal fraction of each phase (plagioclase, oxides, glass matrix), obtaining results consistent within 5 vol%. A few images at higher magnification (150 \times , 450 \times) were also collected and processed, and lead to coherent crystallinity estimates.

Iron redox determination

Concentric cylinder subliquidus experiments, which maintain the samples at magmatic temperatures for about 24 h at atmospheric conditions, may result in sample oxidization. Iron redox state has an influence on melt viscosity, because oxidized melts are slightly more viscous than equivalent reduced melts (Dingwell and Virgo 1988). Therefore, the iron oxidation state of the natural rock and of all the experimental samples was measured to assess the possible influence of iron redox state on magma viscosity. We used a combination of wet chemistry and ultraviolet/visible (UV/Vis) photo-spectrometry, following the method developed by Wilson (1960) and modified by Schuessler et al. (2008) and Sehlke et al. (2014). Full details of the method and calibration are given in Sehlke et al. (2014).

Results

Sample characterization

According to the TAS classification, lavas erupted during the 2014 Pacaya eruption are basalts (Table 2), slightly but consistently lower in alkali (by 0.2 wt%) than recent eruptive products of Pacaya over the years 1996–2010 (Morgan et al. 2013; Robert 2014; Bollasina 2014). The southern flow is slightly more evolved than the western flow, in contrast to

the previous effusive eruption of 2010, when the western flow was more evolved than the southern flow. The measured $\text{Fe}^{2+}/\text{Fe}_{\text{tot}}$ ratio is 0.75 ± 0.05 in all samples.

All samples collected from both flows are mineralogically alike, being constituted of plagioclase and olivine phenocrysts immersed in a microcrystalline matrix of plagioclase and oxides (Fig. 2). All samples collected after cooling contained ~40 % phenocrysts and ~40 % microlites, with ~20 % bubbles and no visible glass. Samples collected from the active southern flow front and quenched with water have a similar bubble content (~20 %) and phenocryst population (~40 %), but fewer microlites (~20 %) and ~20 % interstitial glass instead, indicating that while the phenocrysts are pre-eruptive, about half of the microlites developed during or post-emplacment.

The DRE density of the samples is 2995 kg/m^3 on average, while the bulk density varies from 862 to 2617 kg/m^3 due to porosity ranging from 12 to 70 vol%. The inter-core, intra-sample variability is as high as 1120 kg/m^3 , demonstrating great heterogeneity of bubble content on the cm scale. The western flow shows higher and more variable porosity than the southern flow. If only the samples collected from the levées are considered, a trend of decreasing porosity exists downflow for both flows, while the channel samples do not display a distinct porosity trend. All density and porosity data are reported in Table 3.

Field observations

Active southern flow

The 2014 southern flow was emitted from a vent at an altitude of 1675 m, inside the Pacaya Viejo collapse scar, where all recent flows were located except for the 2010 Los Pocitos flow. This southern flow extended to a length of 4.2 km, and had a well-developed channel in its upper section. Its flow direction from the vent was initially SSW, but a westerly turn was imposed by pre-existing topography at about 3.4 km from the vent (Fig. 1). We were able to record videos of the southern flow activity on January 15th and 16th 2014 at three different locations (Fig. 3a), one near the vent (50 m away), one looking down from the Pacaya Viejo collapse scarp, and one further downstream (600 m away) observing the flow from its western levée. Flow velocities were extracted from the video using Tracker[®], and the viscosity was then calculated using Jeffreys' equation (Jeffreys 1925). The bulk density of the samples measured in the laboratory was $2300 \pm 180 \text{ kg/m}^3$ on average, while the slope and width of the flow were directly measured in the field with the laser rangefinder and varied respectively between 45° and $4 \pm 1 \text{ m}$ upflow, and 4° and $8 \pm 2 \text{ m}$ downflow. Flow depth was more difficult to estimate; the maximum depth was constrained by the levée height (2–5 m), consistently with the commonly used half-flow

Table 2 Geochemical analyses of sample 14PA04 (whole rock) and subliquidus experimental glasses (EMPA). For whole rock (wr) analyses the uncertainty value reported is the average of the difference between the

standards analyses and their certified values. The values provided for glass (gl) microprobe analyses are the average and 2σ standard deviation of 5 analyses each

Sample	14PA04		1234 °C		1228 °C		1224 °C		1211 °C		1199 °C		
	Mineralogy		Spinel + plag + olivine		Spinel plag		Spinel + plag spinel		Spinel + plag spinel		Spinel + plag spinel		
	wr	Uncertainty	gl	stdev	gl	stdev	gl	stdev	gl	stdev	gl	stdev	
SiO ₂	wt%	51.11	0.60	50.91	0.17	51.60	0.24	50.85	0.16	52.52	0.34	52.74	0.28
TiO ₂	wt%	1.12	0.05	1.14	0.03	1.37	0.04	1.33	0.04	1.45	0.03	1.48	0.01
Al ₂ O ₃	wt%	18.36	0.14	19.60	0.16	17.56	0.10	17.66	0.16	17.03	0.19	16.94	0.14
FeO	wt%	11.00	0.00	9.42	0.06	9.33	0.05	9.53	0.09	8.84	0.16	8.93	0.19
MnO	wt%	0.17	0.19	0.16	0.02	0.20	0.01	0.18	0.02	0.20	0.03	0.22	0.02
MgO	wt%	4.12	0.15	4.24	0.04	4.66	0.07	4.68	0.02	5.02	0.07	5.10	0.02
CaO	wt%	9.36	0.07	9.49	0.04	8.68	0.08	8.76	0.04	8.58	0.04	8.49	0.05
Na ₂ O	wt%	3.25	0.01	3.53	0.07	3.67	0.04	3.69	0.02	3.09	0.32	3.34	0.05
K ₂ O	wt%	0.89	0.01	0.90	0.02	1.08	0.04	1.05	0.06	1.13	0.02	1.18	0.03
P ₂ O ₅	wt%	0.24	0.01	0.27	0.02	0.32	0.03	0.34	0.02	0.34	0.01	0.34	0.02
TOTAL	wt%	99.62	0.01	99.67	0.25	98.47	0.16	98.06	0.29	98.22	0.63	98.75	0.36

width approximation (Hulme 1974). Our best depth estimates were 2 ± 1 m near the vent and 4 ± 1 m further downflow. The flow surface velocity in the middle of the flow, extracted from the recorded videos, was 2.8 ± 0.7 m/s upflow, 2.0 ± 0.5 m/s midflow, and 0.3 ± 0.1 m/s downflow (Fig. 3b). Near the vent, where the flow was channelized and still incandescent, this led to a viscosity estimate of 7600 Pa s (between 1900 and 17,100 Pa s including uncertainties). At ~ 175 m away from the vent the flow split briefly into two separate channels, which only slightly perturbed the flow velocity and estimated viscosity. In the more distal part of the flow, 600 m away from the vent, the

viscosity was estimated to have increased to 28,000 Pa s (between 12,300 and 40,200 Pa s including uncertainties). A summary of these calculations is given in Table 4.

Inactive western flow

We visited the 2014 western flow on January 16th 2014, 5 days after it had stopped flowing. The effusion took place from a new vent, located at the base of the SSE-NNW-trending crack that splits the summit edifice of Pacaya, and very close to the 2010 NW vent. While descending the western flank of

Fig. 2 Thin sections in transmitted light (*top*) and BSE (*bottom*) images illustrating the petrography of samples near the vent (14PA04, *left*) and at the flow front (14PA19, *right*). The mineralogy consists of plagioclase and olivine phenocrysts (*pc*) immersed in a microcrystalline (*ml*) matrix of plagioclase and oxides; glass (*gl*) is only present in the sample quenched from the flow front. Bubbles appear *blue* in thin sections and *black* in BSE images

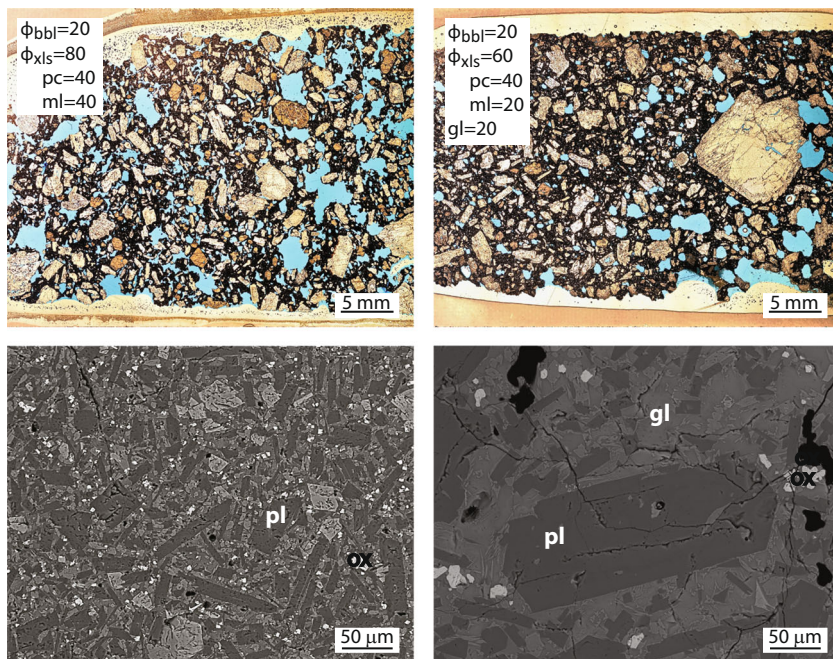


Table 3 Density (geometric, Archimedean, pycnometric) and porosity (φ) of each sample. 2σ variability, when quotable, is based on 5 cores per sample. Porosity is expressed as total (tot), interconnected (int), and isolated (is) (see main text for calculations)

Flow	Sample	Geometric ^a	Variability	Archimedean ^a	Variability	Pycnometric ^a	Total	Interconnected	Isolated
		Density ρ_g kg/m ³	2σ kg/m ³	Density ρ_a kg/m ³	2σ kg/m ³	Density ρ_{DRE} kg/m ³	Porosity φ_{tot}	Porosity φ_{int}	Porosity φ_{is}
Southern	14PA04	2222	222	2606	91	2972	0.25	0.15	0.11
	14PA05	2063	129	2619	77	2949	0.30	0.21	0.09
	14PA06	2157	318	2696	97	2991	0.28	0.20	0.08
	14PA01	2419	293	2857	39	2934	0.18	0.15	0.02
	14PA03	2617	676	2852	134	2968	0.12	0.08	0.04
	14PA17	2379	263	2777	138	2990	0.20	0.14	0.06
	14PA18	2169	142	2758	47	2947	0.26	0.21	0.05
	14PA19	2400	142	2780	15	2992	0.20	0.14	0.06
	Western	14PA07	862	452	2598	109	2913	0.70	0.67
14PA08		1454	286	2521	521	2995	0.55	0.47	0.08
14PA09		1812	222	2560	78	2964	0.39	0.29	0.10
14PA10		2128	676	2563	158	2973	0.27	0.25	0.02
14PA11		1902	286	2491	96	2965	0.36	0.24	0.12
14PA12		2322	329	2677	137	3005	0.25	0.13	0.12
14PA13		2506	71	2691	64	2998	0.20	0.07	0.13
14PA15		2070	537	2630	156	2947	0.30	0.21	0.08
14PA16		1949	149	2378	240	2992	0.35	0.18	0.17
14PA14		2298	103	2633	27	2958	0.22	0.13	0.10

^a Precision (2σ) is better than 20 kg/m³ for geometric density, 200 kg/m³ for Archimedean density, and 51 kg/m³ for pycnometric density

Pacaya, the flow was channelized; upon reaching the plain surrounding the volcano, the lava spread out into a flow front about 500 m wide. The total flow length was about 2.5 km, which is longer than the 1.8 km long 2010 NW flow. We were able to do a number of traverses across the flow at different distances from the vent and therefore to trace topographic profiles of the flow by GPS and laser rangefinder (Fig. 4). In profile 1, i.e. about 300 m from the vent, the apparent width of the main channel is 20 m. However, since the profile was not perfectly perpendicular to the flow, the real channel width was about 16 m, the same as in profiles 2 and 3, situated 1.3 km and 1.8 km from the vent respectively. The internal levée height is between 2 and 4 m. A second, outer set of levées is present in all profiles, suggesting that initial extrusion rates were high, followed by a sustained period of lower extrusion rate. In profile 2, it is possible to see how the 2014 flow briefly split, exposing part of the underlying 2010 flow, before reconnecting downflow.

Liquid viscosity

Viscosity measurements were obtained in the 1555–1150 °C temperature range via concentric cylinder viscometry, and in the 725–655 °C temperature range by parallel plate viscometry, spanning 11 orders of magnitude between

3.02 Pa s and $6.92 \cdot 10^{11}$ Pa s (Table 5). The data were least-squares fitted with the VTF equation (Vogel 1921). The best-fit equation is:

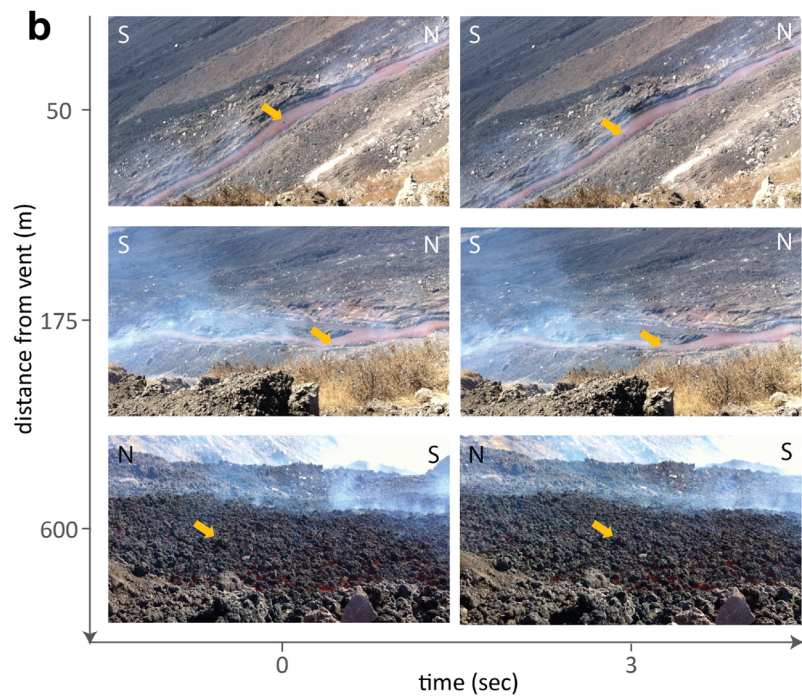
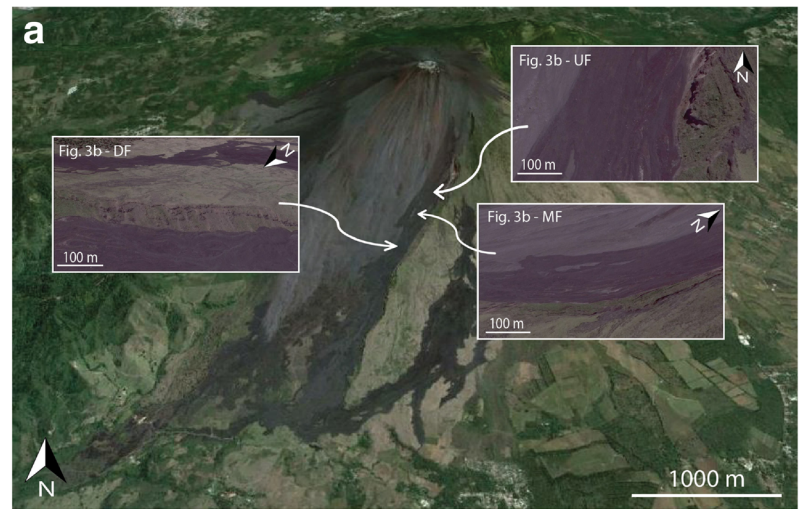
$$\log_{10}\eta = -4.35 + 6071.6/(T-558.3) \quad (12)$$

where T [K] is the temperature. The 34 data points were reproduced with a root-mean-square deviation (RMSD) of 0.06 log units, confirming that no crystallization occurred during the liquid-only concentric cylinder experiment. Existing viscosity models failed to reproduce the data within a factor of 3, with an RMSD of 0.52 log units for the Giordano et al. (2008) model and 0.59 log units for the Hui and Zhang (2007) model (Fig. 5). The fitting allowed us to interpolate the viscosity of the melt at magmatic (subliquidus) conditions, inaccessible to direct measurement because of rapid crystallization. The response of the melt appeared to be Newtonian down to 1150 °C, where crystallization was finally detected.

The best-fit VTF equation (RMSD=0.10 log units) for the viscosity of the evolved composition, based on data collected from both the concentric cylinder and parallel plate viscometer (Table 5) was:

$$\log_{10}\eta = -3.57 + 5030.9/(T-620.8) \quad (13)$$

Fig. 3 **a** Location of video recordings used to extract the southern flow velocity; **b** example frames of videos used to extract flow velocity at each of the three different locations considered. Arrows indicate lava blocks used as tracer particles



The interstitial melt of other subliquidus experimental runs (between 1234 and 1211 °C) was not synthesized, as

Getson and Whittington (2007) showed that evolving melt viscosity along the liquid line of descent typically follows

Table 4 Field viscosity estimates of the 2014 Pacaya south flow at upflow, midflow, and downflow locations shown in Fig. 3

Location	Velocity v m/s	Density ^a ρ kg/m ³	Slope θ °	Depth d m	Stress σ Pa	Strain Rate $\dot{\gamma}$ s ⁻¹	Viscosity η Pa s
Upflow	2.8	2300	45	2 ± 1	32,000 ± 16,000	4.20 ^{+4.20} _{-1.40}	7,600 ^{+9,500} _{-5,700}
Midflow	2.0	2300	30	2 ± 1	22,600 ± 11,300	3.06 ^{+3.06} _{-1.02}	7,400 ^{+9,200} _{-5,500}
Downflow	0.3	2300	4	4 ± 1	6300 ± 1600	0.23 ^{+0.05} _{-0.08}	28,000 ^{+12,200} _{-15,700}

^aBulk density measurements on samples from the southern flow have a 2σ variability of ±360 kg/m³ (Table 3)

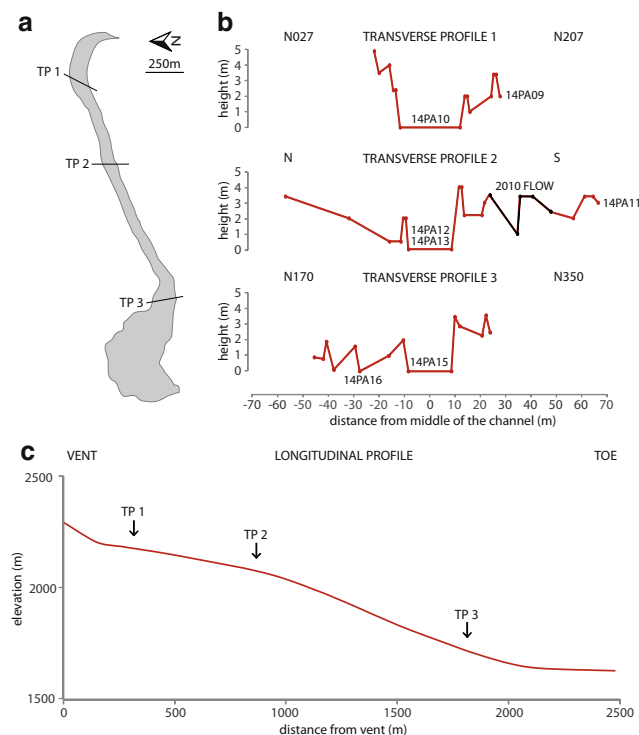


Fig. 4 **a** Location of topographic profiles of the western flow; **b** transverse profiles from laser rangefinder and GPS measurements, with sample locations indicated; **c** longitudinal profile from GoogleEarth®, with transverse profile locations indicated

a quasi-linear trend between the highest and lowest temperatures. Linear interpolation between the melt viscosity at the highest temperature and the evolved melt viscosity at the lowest temperature allowed us to take into account both the temperature and compositional effect when calculating the relative viscosity ($\eta_{rel} = \eta_{mixture} / \eta_{melt}$) for all intermediate temperatures. The uncertainty from making this linear interpolation is small, and comparable to the analytical uncertainty in measurements.

Experimental phase equilibria

Crystallinity of experimental subliquidus runs varies between 0.1 and 40 vol% with decreasing temperatures (from 1234 °C to 1199 °C). The dominant crystalline phase found in the glass matrix is plagioclase, with minor spinel (up to 3.2 vol% at 1199 °C) present. Above a crystallinity of 24 vol% to 35 vol%, plagioclase crystals display a strong preferred orientation (Fig. 6), seen both in the transverse and longitudinal sections.

The measured iron redox state of each subliquidus experimental run was $Fe^{2+}/Fe_{tot} = 0.30 \pm 0.05$ across the whole temperature range (1234–1199 °C). In comparison, the experimental products were more oxidized than the natural rock

($Fe^{2+}/Fe_{tot} = 0.75 \pm 0.05$), leading to the crystallization of oxides instead of olivine.

Subliquidus rheology

Five subliquidus viscosity measurements were performed with the concentric cylinder viscometer; the results are reported in Table 6. SEM images of the 1234 °C run disclosed the presence of a very low crystal fraction (~ 0.001). The lower temperature limit was imposed by the working range of the instrument, which did not allow viscosity measurement below 1199 °C for this composition, due to the high crystal fraction at that temperature. Subliquidus measurements thus had to be restricted to the 1234–1199 °C temperature interval (Fig. 7).

During all subliquidus experiments, a crystallization delay was observed (Fig. 8). The delay was shorter for experiments with greater undercooling (1 h), progressively lengthening in those experiments conducted at temperatures closer to the liquidus (2 h). The viscosity vs. time plots of the two experiments conducted at lowest temperatures (1199 °C and 1211 °C) show that effective viscosity increased for 1–2 h, then peaked and decreased gradually for up to 5 h before achieving steady-state. Rheological data reported in Table 6 were obtained after steady-state effective viscosity had been achieved.

The rheological behavior observed at subliquidus temperatures in our experiments is best described by a power law rheology (Table 7). The consistency value of our experiments (Fig. 9a) increased from 136 Pa s to 1336 Pa s as temperature decreased from 1233 to 1199 °C, while calculated flow indices progressively decreased from 0.94 at 1234 °C to 0.70 at 1199 °C (Fig. 9b), indicating that the degree of shear-thinning increased with decreasing temperatures. The best fits of Eq. 3 returned σ_y values within error of zero, even at the highest crystal fractions.

Discussion

Laboratory constraints on two-phase rheology

Magma is a mixture of three phases: liquid (melt), solid (crystals), and gas (bubbles). One-phase melt viscosity can be predicted knowing its temperature, composition, and water content (Giordano et al. 2008; Hui and Zhang 2007), although not without significant uncertainty (Sehlke et al. 2014). Two-phase viscosity of melt + crystals (Marsh 1981; Pinkerton and Stevenson 1992; Costa et al. 2009; Mueller et al. 2010; Ishibashi and Sato 2007) or melt + bubbles (Manga et al. 1998; Manga and Loewenberg 2001; Rust and Manga 2002; Pal 2003; Llewellyn and Manga 2005; Faroughi and Huber 2015) mixtures has been studied extensively and recently

Table 5 High temperature and near glass transition viscosity measurements of remelted and evolved composition, corresponding to glass quenched from the 1199 °C experiment

Concentric cylinder				Parallel plate			
Temperature	Stress	Strain rate	Viscosity	Temperature	Stress	Strain rate	Viscosity
T	σ	$\dot{\gamma}$	η	T	σ	$\dot{\gamma}$	η
°C	Pa	1/s	Pa s	°C	Pa	1/s	Pa s
Viscosity data for remelt composition							
1554	$1.62 \cdot 10^2$	$5.33 \cdot 10^1$	$3.05 \cdot 10^0$	732.6	$3.82 \cdot 10^5$	$3.75 \cdot 10^{-5}$	$1.02 \cdot 10^{10}$
1530	$1.82 \cdot 10^2$	$4.89 \cdot 10^1$	$3.73 \cdot 10^0$	724.4	$4.02 \cdot 10^5$	$1.26 \cdot 10^{-4}$	$3.19 \cdot 10^9$
1495	$2.23 \cdot 10^2$	$4.44 \cdot 10^1$	$5.02 \cdot 10^0$	720.3	$4.12 \cdot 10^5$	$1.16 \cdot 10^{-4}$	$3.54 \cdot 10^9$
1471	$2.23 \cdot 10^2$	$3.55 \cdot 10^1$	$6.28 \cdot 10^0$	719.6	$3.99 \cdot 10^5$	$3.73 \cdot 10^{-5}$	$1.07 \cdot 10^{10}$
1441	$2.22 \cdot 10^2$	$2.66 \cdot 10^1$	$8.33 \cdot 10^0$	714.8	$4.06 \cdot 10^5$	$7.11 \cdot 10^{-5}$	$5.71 \cdot 10^9$
1415	$1.90 \cdot 10^2$	$1.78 \cdot 10^1$	$1.07 \cdot 10^1$	709.9	$4.05 \cdot 10^5$	$4.26 \cdot 10^{-5}$	$9.53 \cdot 10^9$
1389	$1.23 \cdot 10^2$	$8.88 \cdot 10^0$	$1.39 \cdot 10^1$	703.7	$3.96 \cdot 10^5$	$2.37 \cdot 10^{-5}$	$1.67 \cdot 10^{10}$
1366	$1.98 \cdot 10^2$	$1.11 \cdot 10^1$	$1.78 \cdot 10^1$	700.3	$4.08 \cdot 10^5$	$2.08 \cdot 10^{-5}$	$1.96 \cdot 10^{10}$
1332	$2.26 \cdot 10^2$	$7.77 \cdot 10^0$	$2.91 \cdot 10^1$	693.3	$3.93 \cdot 10^5$	$8.08 \cdot 10^{-6}$	$4.86 \cdot 10^{10}$
1304	$1.81 \cdot 10^2$	$4.44 \cdot 10^0$	$4.08 \cdot 10^1$	689.2	$3.97 \cdot 10^5$	$8.02 \cdot 10^{-6}$	$4.96 \cdot 10^{10}$
1273	$1.34 \cdot 10^2$	$2.22 \cdot 10^0$	$6.02 \cdot 10^1$	684.1	$4.02 \cdot 10^5$	$4.85 \cdot 10^{-6}$	$8.29 \cdot 10^{10}$
1244	$1.59 \cdot 10^2$	$1.78 \cdot 10^0$	$8.94 \cdot 10^1$	678.8	$3.94 \cdot 10^5$	$2.63 \cdot 10^{-6}$	$1.50 \cdot 10^{11}$
1221	$1.67 \cdot 10^2$	$1.33 \cdot 10^0$	$1.25 \cdot 10^2$	674.2	$4.03 \cdot 10^5$	$2.48 \cdot 10^{-6}$	$1.62 \cdot 10^{11}$
1197	$8.02 \cdot 10^1$	$4.44 \cdot 10^{-1}$	$1.81 \cdot 10^2$	669.6	$4.00 \cdot 10^5$	$9.17 \cdot 10^{-7}$	$4.36 \cdot 10^{11}$
1176	$1.14 \cdot 10^2$	$4.44 \cdot 10^{-1}$	$2.56 \cdot 10^2$	661.6	$3.92 \cdot 10^5$	$7.18 \cdot 10^{-7}$	$5.45 \cdot 10^{11}$
1150	$1.88 \cdot 10^2$	$4.44 \cdot 10^{-1}$	$4.23 \cdot 10^2$	655.8	$3.97 \cdot 10^5$	$1.33 \cdot 10^{-7}$	$2.98 \cdot 10^{12}$
				655.5	$4.01 \cdot 10^5$	$5.79 \cdot 10^{-7}$	$6.92 \cdot 10^{11}$
				648.7	$3.79 \cdot 10^5$	$1.57 \cdot 10^{-7}$	$2.42 \cdot 10^{12}$
Viscosity data for evolved composition							
1550	$2.05 \cdot 10^2$	$3.33 \cdot 10^1$	$6.15 \cdot 10^0$	715.8	$3.99 \cdot 10^5$	$2.88 \cdot 10^{-4}$	$3.54 \cdot 10^9$
1477	$1.66 \cdot 10^2$	$2.22 \cdot 10^1$	$7.46 \cdot 10^0$	707.6	$3.99 \cdot 10^5$	$1.85 \cdot 10^{-5}$	$2.16 \cdot 10^{10}$
1450	$3.31 \cdot 10^2$	$3.33 \cdot 10^1$	$9.94 \cdot 10^0$	706.8	$4.01 \cdot 10^5$	$1.75 \cdot 10^{-5}$	$2.30 \cdot 10^{10}$
1400	$2.20 \cdot 10^2$	$1.33 \cdot 10^1$	$1.65 \cdot 10^1$	697.9	$4.01 \cdot 10^5$	$1.07 \cdot 10^{-5}$	$3.76 \cdot 10^{10}$
1351	$2.84 \cdot 10^2$	$9.99 \cdot 10^0$	$2.84 \cdot 10^1$	694.3	$3.96 \cdot 10^5$	$2.69 \cdot 10^{-6}$	$1.47 \cdot 10^{11}$
1301	$2.29 \cdot 10^2$	$4.44 \cdot 10^0$	$5.15 \cdot 10^1$	688.6	$3.97 \cdot 10^5$	$2.18 \cdot 10^{-6}$	$1.82 \cdot 10^{11}$
1252	$2.19 \cdot 10^2$	$2.22 \cdot 10^0$	$9.84 \cdot 10^1$	686.1	$3.97 \cdot 10^5$	$1.36 \cdot 10^{-6}$	$2.92 \cdot 10^{11}$
1202	$1.85 \cdot 10^2$	$8.88 \cdot 10^{-1}$	$208 \cdot 10^2$	676.7	$3.98 \cdot 10^5$	$8.18 \cdot 10^{-7}$	$4.86 \cdot 10^{11}$
				672.2	$3.95 \cdot 10^5$	$5.86 \cdot 10^{-7}$	$6.74 \cdot 10^{11}$

reviewed by Mader et al. (2013). Constitutive models exist for both cases, although models for bubble-bearing magmas (Llewellyn and Manga 2005; Faroughi and Huber 2015) are also based on physical theory, while those for crystal-bearing magmas (Roscoe 1952; Costa et al. 2009) are entirely empirical. Here, we compare our experimental data with previous studies and model predictions in terms of relative viscosity, non-Newtonian behavior, and yield strength.

Relative viscosity

At 1199 °C, the evolved melt was only ~1.1 times more viscous (218 Pa s, VTF fit) than the initial melt composition (196 Pa s, VTF fit). The melt viscosity itself almost doubled

from 113 Pa s for the starting melt at 1234 °C to 218 Pa s for the evolved melt at 1199 °C (Fig. 5). However, the viscosity of the crystal-bearing mixture increased by an order of magnitude, from 136 Pa · s to 1,336 Pa · s, over the same temperature range, as the crystal fraction increased from $\phi_c=0.001$ to $\phi_c=0.40$ (Fig. 7). This demonstrates that, for this lava flow, the chemical effect of melt evolution on magma viscosity was minor compared to the physical effect of crystal growth (Fig. 10).

The relative viscosity of our subliquidus experiments increases with a quasi-linear trend, as do those of Mauna Ulu (Sehlke et al. 2014) and Fuji (Ishibashi and Sato 2010). The viscosity model of Mader et al. (2013) for suspensions containing smooth or rough particles instead predicts a non-linear

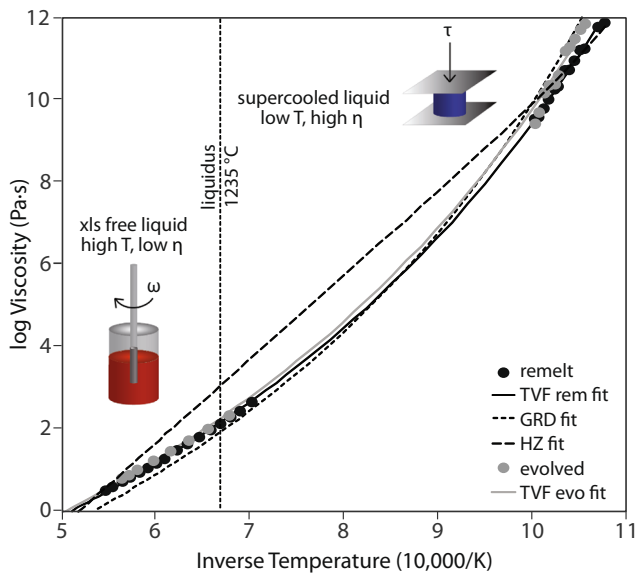


Fig. 5 Viscosity measurements obtained via concentric cylinder (1555–1150 °C) and parallel plate (725–655 °C) viscometry on the remelt (black circles) and evolved (gray circles) compositions. The two data sets are fitted with the VTF equations $\log \eta = -4.40 + 6071/(T - 558.3)$ (remelt composition; continuous black curve) and $\log \eta = -3.57 + 5030/(T - 620.8)$ (evolved composition; continuous gray curve). The viscosities predicted by the Giordano et al. (2008) and Hui and Zhang (2007) models for the remelt composition are shown as well (dashed black curves)

growth trend, and while it fits quite well up to crystallinities <24 %, it overestimates the viscosity of more crystalline samples by one (rough particles) or two (smooth

particles) orders of magnitude (Fig. 9c). This could be due to the fact that the Mader et al. (2013) model is not geared towards poly-disperse suspensions. In our experiments, the plagioclase crystals are noticeably larger than the oxides (Fig. 6). In the natural samples, phenocrysts and microlites coexist as two very distinct size populations (Fig. 2). As shown by Cimarelli et al. (2011), Faroughi and Huber (2014), and Moitra and Gonnermann (2015), direct comparison of mono- and poly-disperse suspensions is not straightforward.

Shear-thinning behavior

The presence of crystals also causes the lava rheology to become non-Newtonian. Previous experiments on the rheology of two-phase (melt+crystals) mafic lavas indicate that threshold values for non-Newtonian behavior onset range from 0.05 (Ishibashi and Sato 2007 on Mt. Fuji basalt) to 0.25 (Ryerson et al. 1988 on picrite). This variability is ascribed to the different mineral assemblages crystallized by each composition. Crystals with high aspect ratio, such as plagioclase, can more promptly induce pseudoplastic behavior, since even a small fraction of acicular crystals engenders interactions among crystals, altering the rheological behavior of the suspension (Cimarelli et al. 2011). The unambiguous detection of pseudoplasticity also depends on the experimental conditions and apparatus sensitivity. In our experiments, pseudoplastic behavior was observed at all temperatures

Fig. 6 Crystal fraction developed by each experimental run. The most abundant phase crystallized is plagioclase (black), with minor oxides (white) present; glass matrix is displayed in gray; the original BSE grayscale is retained. Crystal fraction increases with decreasing temperature. At $\phi > 0.24$ –0.35 plagioclase crystals display a preferred orientation

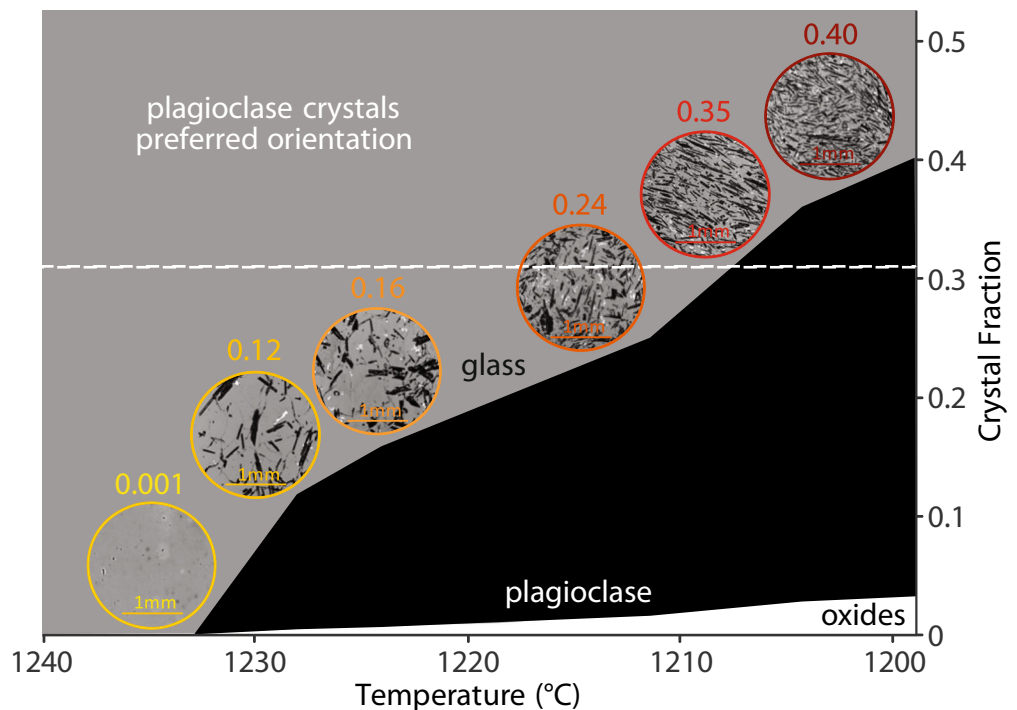


Table 6 Subliquidus stress, strain rate, and viscosity measurements

Concentric cylinder viscosity data at subliquidus temperatures

1234 °C			1228 °C			1224 °C			1211 °C			1199 °C		
Stress	Strain Rate	Viscosity	Stress	Strain Rate	Viscosity	Stress	Strain Rate	Viscosity	Stress	Strain Rate	Viscosity	Stress	Strain Rate	Viscosity
σ	$\dot{\gamma}$	η	σ	$\dot{\gamma}$	η	σ	$\dot{\gamma}$	η	σ	$\dot{\gamma}$	η	σ	$\dot{\gamma}$	η
Pa	1/s	Pa s	Pa	1/s	Pa s	Pa	1/s	Pa s	Pa	1/s	Pa s	Pa	1/s	Pa s
33	0.23	146	93	0.28	331	213	0.26	829	537	0.38	1405	302	0.11	2677
38	0.26	149	192	0.60	322	388	0.54	720	901	0.81	1110	472	0.27	1761
85	0.66	131	273	0.89	307	595	0.90	662	920	0.83	1111	737	0.47	1559
106	0.82	130	339	1.09	311	793	1.26	630	1125	1.08	1039	990	0.70	1412
136	1.05	129	377	1.24	304	874	1.41	619	1385	1.50	925	1354	1.07	1269
160	1.26	127	458	1.46	313	1082	1.77	611	1457	1.67	872	1604	1.34	1195
183	1.43	128	536	1.84	292	1183	1.99	594	1565	1.77	886	1999	1.80	1110
223	1.77	126	581	1.89	308	1287	2.18	590	1665	2.13	780			
258	2.06	125	641	2.11	304	1335	2.34	571	1735	2.36	736			
276	2.21	125	654	2.28	287	1452	2.57	566	1943	2.64	735			
291	2.34	124	701	2.34	299	1578	2.82	559	2022	2.90	698			
295	2.34	126	1347	4.68	288				2121	3.10	683			
437	3.51	124												
579	4.68	124												

where crystals were present; however, a particularly marked increase in the deviation from Newtonian behavior was observed at a crystal fraction between 0.12 and 0.16, where the flow index began to decrease sharply (Fig. 9b).

In contrast to experimental samples, only a very weak crystal alignment was observed in the groundmass of samples collected from the lava flow (Fig. 2). This implies that, while flow appears to be laminar in the uppermost channel section, crystal alignment was achieved neither in the channel nor previously during conduit ascent. Indeed, we calculated that lava would have to flow for at least 50 km in

order to reach the amount of finite strain at which we observed an effective viscosity reduction in our experiments, which we interpreted as being due to crystal alignment. We calculated this distance by multiplying the experimental strain rates of 2.2 s^{-1} by the time gap of at least 2 h between the effective viscosity peak (end of crystallization) and the achievement of a constant effective viscosity (end of crystal alignment) observed in the laboratory experiments (Fig. 8). Lava flows at Pacaya have not exceeded 5.5 km in recent years, therefore their lack of crystal alignment is not surprising.

Fig. 7 Subliquidus viscosity data at 5 temperatures between 1234 °C and 1199 °C, presented in a rheological map (stress vs. strain rate plot). Experimental data are best fit by a power law equation. Lower temperature runs have a higher viscosity and are increasingly non-Newtonian

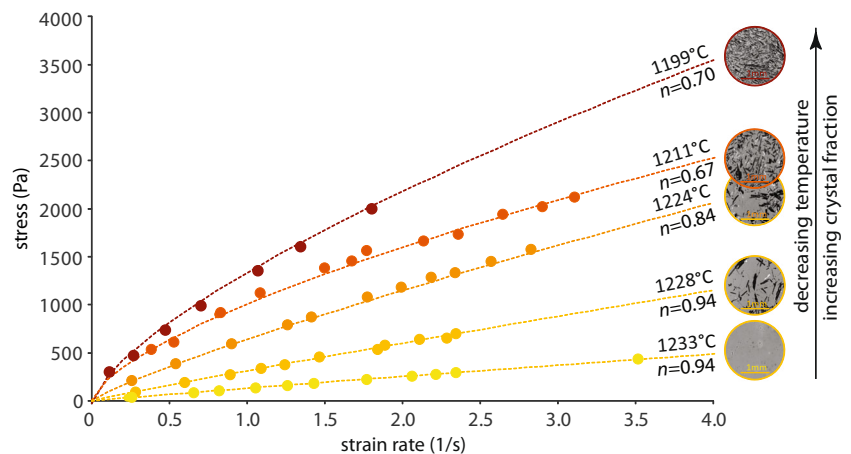
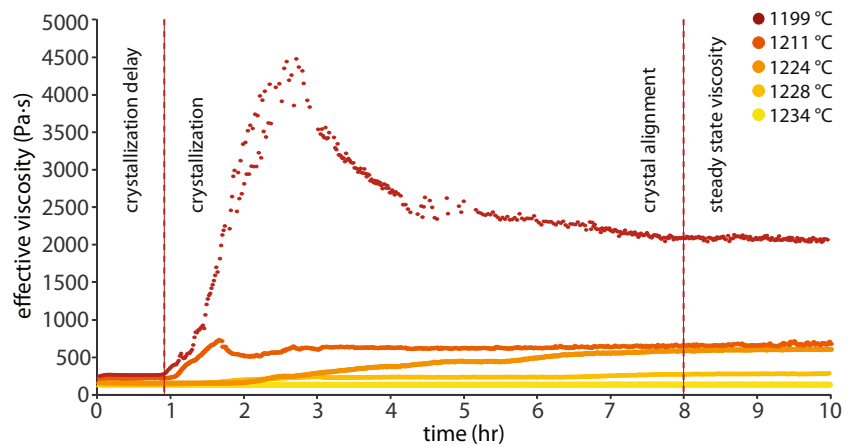


Fig. 8 Plot of effective viscosity vs. time, showing crystallization delay and steady-state effective viscosity achievement in subliquidus experiments



Yield strength

For the 2014 western Pacaya flow, application of Eq. 5 (with $h_c = 2 \pm 1$ m, $\rho = 2,300$ kg/m³, $g = 9.8$ m/s², $\alpha = 45^\circ$) leads to a yield strength estimate of $\sim 45,200 \pm 22,600$ Pa, while use of Eq. 6 (with $w = 1.5 \pm 0.5$ m) results in a yield strength of $\sim 41,700 \pm 13,900$ Pa. The biggest uncertainty is in flow thickness/levée height, so these estimates could be in error by as much as a factor of 2. Near the flow toe, where ground slope was $\sim 3^\circ$, and the flow front was ~ 3 m high, yield strength is estimated at $\sim 340,000$ Pa from Eq. 5. In contrast, laboratory experiments did not reveal a yield strength even at the highest investigated crystal volume fraction of 0.40. Although our laboratory subliquidus rheology data were fit using the Herschel-Bulkley constitutive law, which allows for the existence of a yield strength, the best values returned were always within error of zero. This suggests that yield strength develops between crystal fractions of 0.40 in laboratory experiments and 0.75 of lava dense rock equivalent in the field for this basaltic composition.

Laboratory constraints on three-phase rheology

Few studies have focused on three-phase rheology, where crystals and bubbles coexist in a melt. Truby et al. (2015) developed an effective medium treatment of the issue, in which the bubble suspension is treated as a continuous medium suspending the crystals. Although experimentally validated, this model is only applicable when bubbles are smaller than crystals, which is often not the case in magmas, and does not apply to the lava flows at Pacaya. Phan-Thien and Pham (1997) obtained the viscosity of three-phase mixtures via a multi stage process in which a series of incremental additions of crystals and bubbles of various sizes to a starting melt allows to calculate the effective viscosity of the mixture at each step, and to use it as a starting point for the next step. The model is limited in that it is based on a single strain rate of 1 s⁻¹ and treats bubbles as rigid spheres, so that

bubbles should always increase the mixture bulk viscosity. However, for 2014 Pacaya lavas the melt+crystal viscosity measured in the laboratory is already higher than the three-phase viscosity predicted by the Phan-Thien and Pham (1997) model, which points to the model underestimating viscosity. The strain rate variation between 4.2 and 0.2 s⁻¹, together with the presence of crystals with two distinct size populations, may at least partially explain this discrepancy. However, it is likely that the model simply cannot be applied to lavas with such a high crystallinity and high viscosity. For the 2014 eruption at Pacaya, we can turn to field observations to place constraints on three-phase rheological behavior.

Field constraints on three-phase rheology

Viscosity in both the upper channel and `a`a portions of the flow was estimated from the video recordings. Effective viscosity estimates were influenced by slope, density, and depth; stress was calculated from the measured density, measured ground slope, and assumed depth, and strain rate was calculated from the observed velocity and an assumed depth. The estimated effective viscosity was $7,600^{+9,500}_{-5,700}$ Pa s upflow, which increased by a factor of 3.7 to $28,000^{+12,200}_{-15,700}$ Pa s only ~ 550 m downflow.

Table 7 Fitting parameters for subliquidus experiments flows curves and relative standard deviations (2σ)

Temperature	Crystal fraction	Flow index	Consistency	Yield strength
T °C	ϕ_c	n	K Pa s	σ_y Pa
1199 ± 0.1	0.40 ± 0.01	0.70 ± 0.05	1336 ± 50	-36 ± 46
1211 ± 0.1	0.24 ± 0.02	0.67 ± 0.03	990 ± 49	39 ± 71
1224 ± 0.3	0.16 ± 0.01	0.84 ± 0.01	663 ± 12	-5 ± 20
1228 ± 0.4	0.12 ± 0.01	0.94 ± 0.02	316 ± 7	-6 ± 14
1234 ± 0.2	0.001 ± 0.00	0.94 ± 0.01	136 ± 2	-6 ± 4

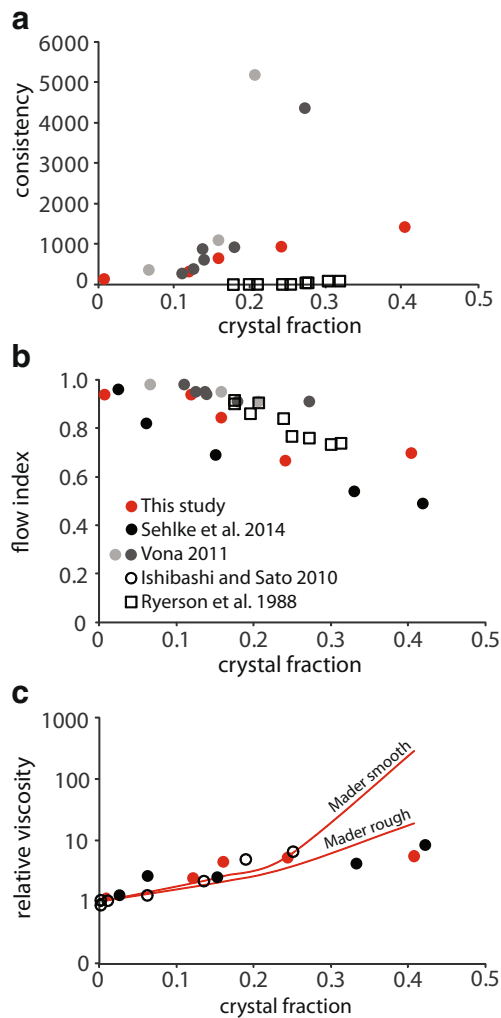


Fig. 9 Variations of **a** consistency (K), **b** flow index (n), and **c** relative viscosity (η_{rel}) as a function of crystal fraction for 2014 Pacaya lavas (red circles), compared with other studies (black and gray symbols). In **c** we also plot the predictions of the Mader et al. (2013) algorithm using an aspect ratio of 5, both for rough and smooth particles

A direct temperature measurement is not available for the 2014 eruption, but upflow thermocouple-based temperature measurements of the compositionally similar 2010 flow by one of us [G.C.] are around 1200 °C. Comparison of crystal fraction in natural and experimental samples collected from the 2014 eruption also lead to an estimate of about 1200 °C. Although the surface temperature of the flow clearly decreased from the incandescent magma fully exposed near the vent to the colder blocks towards the toe, the flow interior probably remained thermally insulated. While lava flows do not develop a proper crust, the top blocks cool down quickly in contact with the air, and subsequently prevent the core of the flow from radiating the majority of its heat.

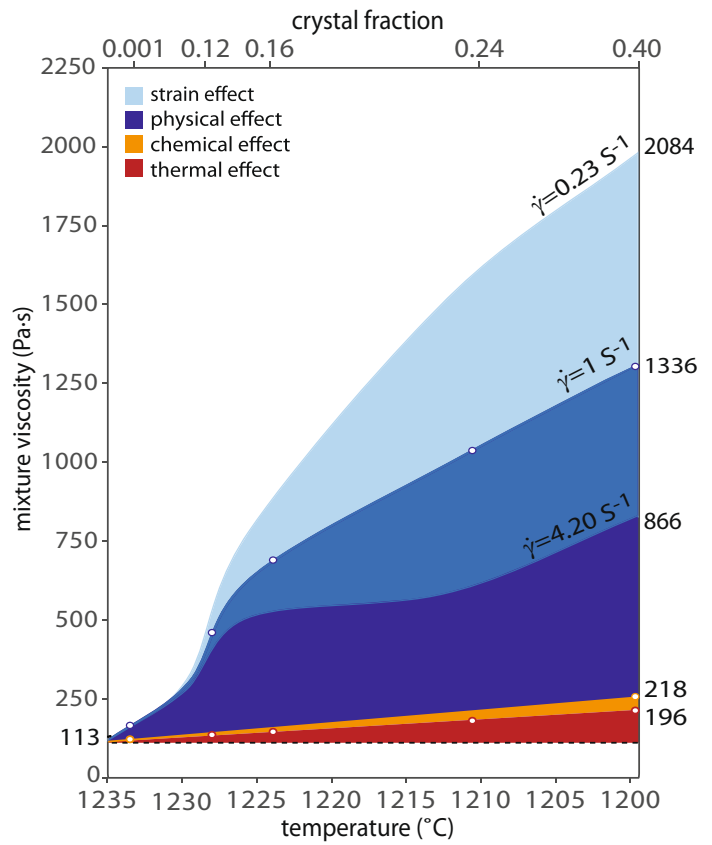
Comparison with experimental data collected at 1199 °C (Fig. 11), pertinent to the upper channel conditions, indicates that the decrease in ground slope from 45° at 50 m from the vent to 4° at 600 m from the vent should result in a factor of

2.9 increase in effective viscosity, simply due to pseudoplastic behavior. This was calculated by noting that when the strain rate in the experiment was 4.2 s⁻¹, corresponding to the observed strain rate near the vent at Pacaya, the effective stress in the experiment was 3637 Pa, and the effective viscosity was 866 Pa s. Reducing the effective stress by a factor of 11.25, equivalent to reducing the slope from 45° to 4°, resulted in a predicted strain rate of 0.13 s⁻¹ and an effective viscosity of 2476 Pa s, an increase of 2.9 times. Strain estimates based on Jeffreys' equation for the studied downflow location yield a slightly higher strain rate of 0.23 s⁻¹ due to flow depth increase. The additional increase in effective viscosity observed between the proximal and distal locations must have resulted from cooling and crystallization.

The factor of 2.9 is a minimum constraint on the effect of ground slope on viscosity, because the degree of non-Newtonian behavior increases with crystal fraction. The additional factor of 1.3 viscosity increase observed, corresponding to 6054 Pa s, could result entirely from cooling of 70 °C, based on the VTF equation for the evolved liquid. This is a maximum estimate of the amount of cooling, because any temperature decrease should also result in an increase in crystal fraction, which would in turn increase the viscosity. Alternatively, this additional viscosity increase of 6054 Pa s could result entirely from further crystallization of an already undercooled melt. A combination of cooling and crystallization is the most likely possibility. As in the laboratory experiments, the chemical effect of evolving residual melt of the flow is expected to be negligible compared to the physical effects of decreasing strain rate and increasing crystal fraction. We conclude that pre-existing topography has a fundamental role in determining flow rheology, by affecting the stress and strain rate imposed on the lava. For the 2014 southern Pacaya flow, strain rate decrease accounts for most of the observed effective viscosity increase, at least within our observation range (between 50 and 600 m from the vent).

Bubbles are also omnipresent in the flow, and they can be expected to significantly affect the lava rheology. As shown by Llewellyn and Manga (2005), *soft*, deformed bubbles such as those observed in our natural samples form in response to a fluid dynamic regime in which viscous forces prevail over surface tension forces (capillary number $Ca > 1$). Specifically, we calculate a range of capillary numbers of $2 < Ca < 73$, based on the strain rates estimated in the field, effective viscosities measured in the laboratory at 1200 °C, and the observed bubble sizes (1–5 mm). Hence, the presence of bubbles should result in a decrease in the effective bulk viscosity of the lava of up to 50 % (Llewellyn and Manga 2005). The bubble population is extremely heterogeneous throughout the flow, as highlighted by the significant variability of density even within individual samples (Table 3). As a consequence, we speculate that large viscosity variations must exist at the local (cm to m) scale. However, we do not observe

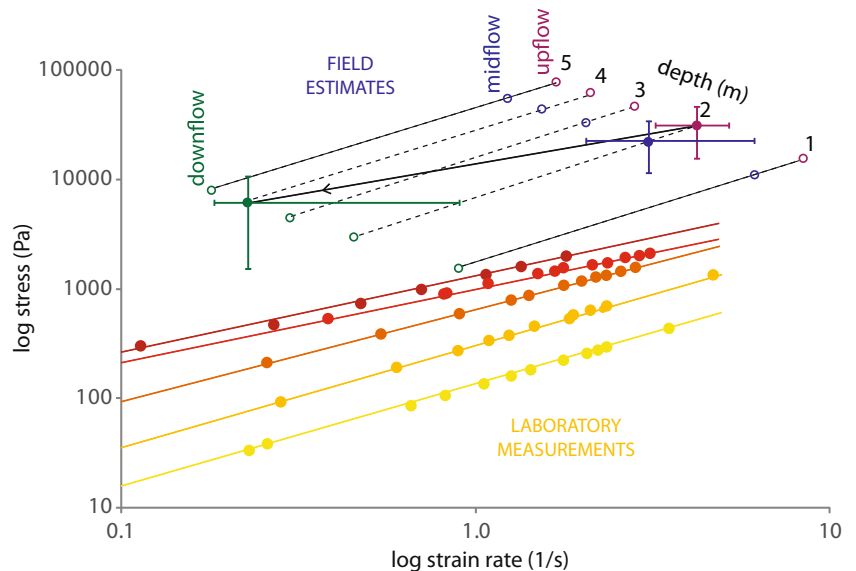
Fig. 10 Viscosity of 2014 Pacaya lavas at a strain rate of 1 s^{-1} (unless otherwise specified) as a function of temperature and crystallinity. Remelt composition is shown in red, evolved composition in orange, and two-phase (melt + crystals) mixture in different shades of blue depending on the specified strain rates considered, comprised between the highest (4.20 s^{-1}) and lowest (0.23 s^{-1}) values estimated in the field



any systematic increase or decrease in the bubble fraction, size, or shape (thin sections observations) downflow. We therefore assume that the effect of bubbles on the rheology of the flow is similar for both the upflow and downflow sections. This assumption allows us to infer the relative effects of cooling, chemical evolution, crystallization, and slope decrease along the lava flow. The rheological effect of bubbles certainly

causes a discrepancy between field- and laboratory- based viscosity estimates. However, as shown by Fig. 11, field-based (bubble rich) viscosity estimates are higher than laboratory-based (bubble free) measurements. It is therefore apparent that the lower temperature and higher crystallinity which characterize lava in the field play a more prominent role than bubbles in determining its rheology. It is interesting

Fig. 11 Log stress vs. log strain rate plot showing subliquidus experimental data (yellow to red color shades) compared to viscosity estimates based on field measurements (data in Table 4). A range of plausible depths is presented for field estimates, and the most likely viscosity path is shown (solid black line)



to note that the isothermal flow curves measured in the laboratory and the preferred path estimated from the field observations are almost parallel (Fig. 11), substantiating the utility of integrating the two techniques when studying the rheology of a lava flow.

Conclusions

Through the integration of field observations and laboratory experiments, we assessed how the rheological properties of the January 2014 Pacaya lava flows evolved both in space and time. In the laboratory, we measured the rheology of lava during cooling and crystallization from 1234 °C to 1199 °C, and we observed increasing viscosity and increasing shear-thinning behavior with increasing crystal fraction. In the field, we estimated a 3.7-fold effective viscosity increase, from ~7,600 Pa s to ~28,000 Pa s, of a flow erupted at ~1200 °C. Our laboratory and field measurements are complementary, as they span contiguous temperature ranges. Accounting for the differences in crystal and bubble fraction, the two data sets are mutually consistent. We show that near the vent, the rheological behavior of the studied flow was mainly controlled by the influence of pre-existing topography. By analogy with experimentally determined constitutive relations, we calculated that the slope reduction accounts for about a 2.9× increase in effective viscosity, while cooling and crystallization account for no more than a 1.3× increase. Our results should apply qualitatively to other volcanoes with dramatic variations in slope, especially for high crystallinity lavas that display shear-thinning behavior. Furthermore, our results reinforce the necessity of incorporating the complex relations between slope, flow velocity and lava rheology into models of lava flow emplacement.

Acknowledgments This research was supported by the National Science Foundation grant EAR-1220051. Logistical support in Guatemala was provided by Instituto Nacional de Sismología, Vulcanología, Meteorología e Hidrología (INSIVUMEH); in particular we thank INSIVUMEH Director Don Eddy Sanchez Bennett, and volcano observers Pastor and Luiz. José was our guide on the flows. Paul Carpenter assisted us with microprobe analyses at Washington University in St. Louis. We are grateful to reviewers Einat Lev and Ed Llewellyn for their thorough and constructive comments, which greatly contributed to improving this paper.

References

- Armstrong JT (1995) CITZAF: a package of correction programs for the quantitative electron microbeam X-ray analysis of thick polished materials, thin films, and particles. *Microbeam Anal* 4:177–200
- Avard G, Whittington AG (2012) Rheology of arc dacite lavas: experimental determination at low strain rates. *Bull Volcanol* 74(5):1039–1056. doi:10.1007/s00445-012-0584-2
- Bardintzeff JM, Deniel C (1992) Magmatic evolution of Pacaya and Cerro Chiquito volcanological complex, Guatemala. *Bull Volcanol* 54(4):267–283. doi:10.1007/BF00301482
- Barnes HA (1999) The yield stress—a review or ‘παντα ρει’—everything flows? *J Nonnewt Fluid Mech* 81(1):133–178. doi:10.1016/S0377-0257(98)00094-9
- Bollasina AJ (2014) The May 2010 eruption of Pacaya volcano, Guatemala: An experimental study of subliquidus magma rheology. M.S. Thesis, University of Missouri
- Cimarelli C, Costa A, Mueller S, Mader HM (2011) Rheology of magmas with bimodal crystal size and shape distributions: Insights from analog experiments. *Geochem Geophys Geosyst* 12(7). doi:10.1029/2011GC003606
- Costa A, Caricchi L, Bagdassarov N (2009) A model for the rheology of particle-bearing suspensions and partially molten rocks. *Geochem Geophys Geosy* 10(3). doi:10.1029/2008GC002138
- Dingwell DB (1995) Viscosity and Anelasticity of Melts. *Mineral Physics & Crystallography: A Handbook of Physical Constants* 209–217. doi:10.1029/RF002p0209
- Dingwell DB, Virgo D (1988) Viscosities of melts in the Na₂O-FeO-Fe₂O₃-SiO₂ system and factors controlling relative viscosities of fully polymerized silicate melts. *Geochim Cosmochim Acta* 52(2):395–403. doi:10.1016/0016-7037(88)90095-6
- Eggers AA (1971) The geology and petrology of the Amatitlán quadrangle, Guatemala. Dissertation, Dartmouth College
- Faroughi SA, Huber C (2014) Crowding-based rheological model for suspensions of rigid bimodal-sized particles with interfering size ratios. *Phys Rev E* 90(5):052303. doi:10.1103/PhysRevE.90.052303
- Faroughi SA, Huber C (2015) A generalized equation for rheology of emulsions and suspensions of deformable particles subjected to simple shear at low Reynolds number. *Rheol Acta* 54(2):85–108. doi:10.1007/s00397-014-0825-8
- Fink JH, Zimbelman JR (1986) Rheology of the 1983 Royal Gardens basalt flows, Kilauea volcano, Hawaii. *Bull Volcanol* 48(2–3):87–96. doi:10.1007/BF01046544
- Gauthier F (1973) Field and laboratory studies of the rheology of Mount Etna lava. *Philos Trans R Soc A* 274(1238):83–98. doi:10.1098/rsta.1973.0028
- Getson JM, Whittington AG (2007) Liquid and magma viscosity in the anorthite-forsterite-diopside-quartz system and implications for the viscosity-temperature paths of cooling magmas. *J Geophys Res-Sol Ea* (1978–2012), 112(B10). doi:10.1029/2006JB004812
- Ghiorso MS, Sack RO (1995) Chemical mass transfer in magmatic processes IV. A revised and internally consistent thermodynamic model for the interpolation and extrapolation of liquid–solid equilibria in magmatic systems at elevated temperatures and pressures. *Contrib Mineral Petrol* 119(2–3):197–212. doi:10.1007/BF00307281
- Giordano D, Russell JK, Dingwell DB (2008) Viscosity of magmatic liquids: a model. *Earth Planet Sci Lett* 271(1):123–134. doi:10.1016/j.epsl.2008.03.038
- Griffiths RW (2000) The dynamics of lava flows. *Annu Rev Fluid Mech* 32(1):477–518. doi:10.1146/annurev.fluid.32.1.477
- Hon K, Gansecki C, Kauahikaua J (2003) The transition from ‘a‘ā to pāhoehoe crust on flows emplaced during the Pu‘u ‘Ō‘ō-Kūpaianaha eruption. In: Heliker C, Swanson DA, Takahashi TJ (eds) *The Pu‘u ‘Ō‘ō-Kūpaianaha eruption of Kilauea Volcano, Hawai‘i: the first 20 years*, vol 1676, U S Geol Surv Prof Pap., pp 63–87
- Hui H, Zhang Y (2007) Toward a general viscosity equation for natural anhydrous and hydrous silicate melts. *Geochim Cosmochim Acta* 71(2):403–416. doi:10.1016/j.gca.2006.09.003
- Hulme G (1974) The interpretation of lava flow morphology. *Geophys J Int* 39(2):361–383. doi:10.1111/j.1365-246X.1974.tb05460.x
- Ishibashi H (2009) Non-Newtonian behavior of plagioclase-bearing basaltic magma: subliquidus viscosity measurement of the 1707 basalt

- of Fuji volcano, Japan. *J Volcanol Geotherm Res* 181(1):78–88. doi:10.1016/j.jvolgeores.2009.01.004
- Ishibashi H, Sato H (2007) Viscosity measurements of subliquidus magmas: alkali olivine basalt from the Higashi-Matsuura district, Southwest Japan. *J Volcanol Geotherm Res* 160(3):223–238. doi:10.1016/j.jvolgeores.2006.10.001
- Ishibashi H, Sato H (2010) Bingham fluid behavior of plagioclase-bearing basaltic magma: reanalyses of laboratory viscosity measurements for Fuji 1707 basalt. *J Mineral Petrol Sci* 105(6):334–339. doi:10.2465/jmps.100611
- Jeffreys H (1925) The flow of water in an inclined channel of rectangular section. *Philos Mag* 49:793–807. doi:10.1080/14786442508634662
- Lev E, James MR (2014) The influence of cross-sectional channel geometry on rheology and flux estimates for active lava flows. *Bull Volcanol* 76:1–15. doi:10.1007/s00445-014-0829-3
- Lev E, Spiegelman M, Wysocki RJ, Karson JA (2012) Investigating lava flow rheology using video analysis and numerical flow models. *J Volcanol Geotherm Res* 247:62–73. doi:10.1016/j.jvolgeores.2012.08.002
- Llewellyn EW, Manga M (2005) Bubble suspension rheology and implications for conduit flow. *J Volcanol Geotherm Res* 143(1):205–217. doi:10.1016/j.jvolgeores.2004.09.018
- Mader HM, Llewellyn EW, Mueller SP (2013) The rheology of two-phase magmas: a review and analysis. *J Volcanol Geotherm Res* 257:135–158. doi:10.1016/j.jvolgeores.2013.02.014
- Manga M, Loewenberg M (2001) Viscosity of magmas containing highly deformable bubbles. *J Volcanol Geotherm Res* 105(1):19–24. doi:10.1016/S0377-0273(00)00239-0
- Manga M, Castro J, Cashman KV, Loewenberg M (1998) Rheology of bubble-bearing magmas. *J Volcanol Geotherm Res* 87(1):15–28. doi:10.1016/S0377-0273(98)00091-2
- Marsh BD (1981) On the crystallinity, probability of occurrence, and rheology of lava and magma. *Contrib Mineral Petrol* 78(1):85–98. doi:10.1007/BF00371146
- Matias Gomez RO (2009) Volcanological Map of the 1961–2009 eruption of Volcan de Pacaya, Guatemala. Dissertation, Michigan Technological University
- Moitra P, Gonnermann HM (2015) Effects of crystal shape-and size-modality on magma rheology. *Geochem Geophys Geosyst* 16(1):1–26. doi:10.1002/2014GC005554
- Moore HJ, Arthur DWG, Schaber GG (1978) Yield strengths of flows on the Earth, Mars, and Moon. *P Lunar Planet Sci C* 9:3351–3378
- Morgan HA, Harris AJ, Gurioli L (2013) Lava discharge rate estimates from thermal infrared satellite data for Pacaya Volcano during 2004–2010. *J Volcanol Geotherm Res* 264:1–11. doi:10.3390/rs8010073
- Mueller S, Llewellyn EW, Mader HM (2010) The rheology of suspensions of solid particles. *P Roy Soc A Math Phys* 466(2116):1201–1228. doi:10.1098/rspa.2009.0445
- Mueller S, Llewellyn EW, Mader HM (2011) The effect of particle shape on suspension viscosity and implications for magmatic flows. *Geophys Res Lett* 38(13). doi:10.1029/2011GL047167
- Pal R (2003) Rheological behavior of bubble-bearing magmas. *Earth Planet Sci Lett* 207(1):165–179. doi:10.1016/S0012-821X(02)01104-4
- Peterson DW, Tilling RI (1980) Transition of basaltic lava from pahoehoe to aa, Kilauea Volcano, Hawaii: field observations and key factors. *J Volcanol Geotherm Res* 7(3):271–293. doi:10.1016/0377-0273(80)90033-5
- Phan-Thien N, Pham DC (1997) Differential multiphase models for polydispersed suspensions and particulate solids. *J Non-Newton Fluid* 72(2):305–318. doi:10.1016/S0377-0257(97)90002-1
- Pinkerton H, Norton G (1995) Rheological properties of basaltic lavas at sub-liquidus temperatures: laboratory and field measurements on lavas from Mount Etna. *J Volcanol Geotherm Res* 68(4):307–323. doi:10.1016/0377-0273(95)00018-7
- Pinkerton H, Stevenson RJ (1992) Methods of determining the rheological properties of magmas at sub-liquidus temperatures. *J Volcanol Geotherm Res* 53(1):47–66. doi:10.1016/0377-0273(92)90073-M
- Robert G (2014) The effects of volatiles on the viscosity and heat capacity of calc-alkaline basaltic and basaltic andesite liquids. Dissertation, University of Missouri-Columbia
- Robert B, Harris A, Gurioli L, Médard E, Sehlke A, Whittington AG (2014) Textural and rheological evolution of basalt flowing down a lava channel. *Bull Volcanol* 76(6):1–21. doi:10.1007/s00445-014-0824-8
- Roscoe R (1952) The viscosity of suspensions of rigid spheres. *Br J Appl Phys* 3(8):267
- Rose WI, Palma JL, Wolf RE, Gomez RO (2013) A 50 yr eruption of a basaltic composite cone: Pacaya, Guatemala. *Geol Soc Am* 498:1–21. doi:10.1088/0508-3443/3/8/306
- Rust AC, Manga M (2002) Bubble shapes and orientations in low Re simple shear flow. *J Colloid Interf Sci* 249(2):476–480. doi:10.1006/jcis.2002.8292
- Ryerson FJ, Weed HC, Piwinski AJ (1988) Rheology of subliquidus magmas: 1. Picritic compositions. *J Geophys Res-Sol Ea* (1978–2012) 93(B4):3421–3436. doi:10.1029/JB093iB04p03421
- Schaefer LN, Oommen T, Corazzato C, Tibaldi A, Escobar-Wolf R, Rose WI (2013) An integrated field-numerical approach to assess slope stability hazards at volcanoes: the example of Pacaya, Guatemala. *Bull Volcanol* 75(6):1–18. doi:10.1007/s00445-013-0720-7
- Schuessler JA, Botcharnikov RE, Behrens H, Misiti V, Freda C (2008) Amorphous materials: properties, structure, and durability: oxidation state of iron in hydrous phono-tephritic melts. *Am Mineral* 93(10):1493–1504. doi:10.2138/am.2008.2795
- Sehlke A, Whittington AG, Robert B, Harris A, Gurioli L, Médard E (2014) Pahoehoe to aa transition of Hawaiian lavas: an experimental study. *Bull Volcanol* 76(11):1–20. doi:10.1007/s00445-014-0876-9
- Shaw HR, Wright TL, Peck DL, Okamura R (1968) The viscosity of basaltic magma; an analysis of field measurements in Makaopuhi lava lake, Hawaii. *Am J Sci* 266(4):225–264. doi:10.2475/ajs.266.4.225
- Sparks RSJ, Pinkerton H, Hulme G (1976) Classification and formation of lava levees on Mount Etna, Sicily. *Geology* 4(5):269–271. doi:10.1130/0091-7613(1976)4<269:CAFOLL>2.0.CO;2
- Spera FJ (2000) Physical properties of magmas. In: Sigurdsson H, Houghton BF, McNutt SR, Rymer H, Stix J, McBirney AR (eds) *Encyclopedia of volcanoes*. Academic Press, San Diego, pp 171–190
- Truby JM, Mueller SP, Llewellyn EW, Mader HM (2015) The rheology of three-phase suspensions at low bubble capillary number. *Proc Roy Soc Lond A Mat* 471(2173):20140557. doi:10.1098/rspa.2014.0557
- Vallance JW, Siebert L, Rose WI, Girón JR, Banks NG (1995) Edifice collapse and related hazards in Guatemala. *J Volcanol Geotherm Res* 66(1):337–355. doi:10.1016/0377-0273(94)00076-S
- Vogel H (1921) The law of the relation between the viscosity of liquids and the temperature. *Z Phys* 22:645–646
- Webb SL, Dingwell DB (1990) The onset of non-Newtonian rheology of silicate melts. *Phys Chem Miner* 17(2):25–132. doi:10.1007/BF00199663
- Whittington AG, Hellwig BM, Behrens H, Joachim B, Stechern A, Vetere F (2009) The viscosity of hydrous dacitic liquids: implications for the rheology of evolving silicic magmas. *Bull Volcanol* 71(2):185–199. doi:10.1007/s00445-008-0217-y
- Wilson AD (1960) The micro-determination of ferrous iron in silicate minerals by a volumetric and a colorimetric method. *Analyst* 85(1016):823–827. doi:10.1039/AN9608500823